Vortex structures in photodetachment by few-cycle circularly polarized pulses

Lei Geng [1], F. Cajiao Vélez [2,*], J. Z. Kamiński [2], Liang-You Peng [1,3,†] and K. Krajewska [2,‡]

[1] *State Key Laboratory for Mesoscopic Physics and Frontiers Science Center for Nano-optoelectronics, School of Physics, Peking University, 100871 Beijing, China*

[2] *Institute of Theoretical Physics, Faculty of Physics, University of Warsaw, Pasteura 5, 02-093 Warsaw, Poland*

[3] *Collaborative Innovation Center of Extreme Optics, Shanxi University, 030006 Taiyuan, China*

(Received 14 July 2020; revised 29 September 2020; accepted 2 October 2020; published 27 October 2020)

Generation of electron vortices in photodetachment of H^- by circularly polarized laser pulses is analyzed by means of strong-field approximation and by numerically solving the time-dependent Schrödinger equation. A very good agreement is shown for the magnitude and the phase of the probability amplitude of photodetachment from both approaches. We demonstrate that spiral-like patterns in the probability amplitude of detachment, observed for a pair of counter-rotating circularly polarized laser pulses, cannot be associated with nonvanishing topological charge vortices. The latter can be generated, on the other hand, by a circularly polarized laser pulse or a sequence of such pulses with corotating polarizations. Such interpretation of our results follows from the hydrodynamical formulation of quantum mechanics and its generalization to arbitrary parametric spaces.

DOI: 10.1103/PhysRevA.102.043117

I. INTRODUCTION

In recent years, an increased interest has been shown to investigate the generation of electron vortices in photoionization. In Ref. [1], for instance, the authors analyzed a single-electron photoionization of He by a sequence of two counter-rotating, circularly polarized attosecond pulses. Their study showed that photoelectron momentum distributions exhibit a helixlike structure, with maximal and minimal probabilities following a *Fermat spiral*. The precise shape of the spiral depends on the time delay between pulses and their relative carrier-envelope phase. As argued, nonzero carrier-envelope phases and long time delays lead to dense helices for which vortices can be observed. Similar dependence on laser field parameters has been seen in the case of diffraction-interference patterns arising in fundamental processes of quantum electrodynamics [2] and in ionization [3]. Based on the analysis presented in Refs. [2,3], one can anticipate that helical and vortex structures in photoelectron momentum distributions are also due to the diffraction and interference of quantum-mechanical probability amplitudes associated with each pulse. Furthermore, it has been shown in Ref. [4] that the number of "spiral arms" depends on the number of photons absorbed from the laser field, provided that each pulse is long enough. On the contrary, vortices discussed in the current paper are not referred to helical patterns mentioned in Refs. [1,4], but to a local structure of the phase. The latter has been analyzed in both position and momentum space in atomic and electronic collisions [5,6], where it was related to the angular momentum transfer. Naturally, one may expect that helical probability distributions might be associated with nonvanishing topological charge vortices. However, only a detailed analysis of the phase of the probability amplitude of the process can truly identify quantum vortex structures.

As we will show in this paper, spiral distributions *do not* always lead to nonvanishing topological charge vortex structures. This is important in light of various works that were stimulated by Ref. [1]. Similar analyses have been carried out, for instance, for double ionization of He [7]. These studies were extended to photoionization of diatomic or triatomic ionic molecules as H_2^+ [8] and H_3^{2+} [9] driven by bichromatic laser pulses in the corotating or counter-rotating configurations. In both cases, helical patterns with single and multiple arms (depending on the relative frequency of the driving field or its helicity) in the photoelectron distributions were predicted. Interference effects in such distributions were also analyzed.

Pengel *et al.* [10] reported on experimental evidence of spiral-like structures in the electron momentum distribution when considering ionization of K atoms by circularly polarized, time-delayed pulses. In Ref. [11], two supercontinuum light pulses with different central frequencies were used to ionize Na atoms. Special attention was paid to the symmetry of the resulting momentum distribution as interpreted by interference effects among electron wave packets with different quantum numbers. Even though the above-mentioned experiments revealed the spiral-type photoelectron momentum distributions, their actual vortex structure remains to be confirmed.

Our aim here is to study the formation of vortex structures in the momentum space during photodetachment of H^- anion (s electron). To this end, we calculate the probability amplitude of detachment from the strong-field approximation (SFA) [12–14] and, independently, by numerically solving the time-dependent Schrödinger equation (TDSE). Note that,

*Felipe.Cajiao-Velez@fuw.edu.pl
†liangyou.peng@pku.edu.cn
‡Katarzyna.Krajewska@fuw.edu.pl

in contrast to photoionization, in photodetachment the electron does not interact with the long-range Coulomb potential created by a positively charged parent ion. For this reason, we expect that the SFA (which for this particular system is also gauge invariant [15]) will lead to accurate qualitative and quantitative predictions. For our numerical illustrations, we choose a driving field consisting of single or double laser pulses with corotating or counter-rotating circular polarizations. We analyze the phase of the resulting momentum probability amplitude and the circulation around its nodal points in order to determine whether or not nonvanishing topological charge vortices are formed. It is worth mentioning that, in Refs. [15–17], the generation of *propagating* electron Bessel states in photoionization (or photodetachment) was studied. However, vortices in the momentum space analyzed in this paper are very different entities. In contrast to the treatment developed there (which was based on the properties of Bessel states in the configuration space), we carry out our analysis under the scope of the hydrodynamical formulation of quantum mechanics.

This paper is organized as follows. In Sec. II, we describe the general properties of electron vortex in the configuration space and their generalization to other parametric spaces. In Sec. III, we introduce the probability amplitude of detachment under the scope of both the SFA and TDSE. In Sec. III A, we define the topological charge of the resulting electron wave packets. As mentioned above, we consider three types of circularly polarized laser fields: a single pulse and two pulses with either corotating or counter-rotating polarizations. Their properties are described in Sec. III B. Numerical results obtained from SFA and TDSE are compared in Sec. IV. Section IV A contains a detailed analysis of the magnitude and phase of the detachment probability amplitude for the driving fields considered here. We determine the regions in the momentum space where vortices are formed. In Sec. IV B, we calculate the topological charge of final electrons. In Sec. V, we compare SFA results for different pulse intensities. Finally, we draw our conclusions in Sec. VI.

Unless stated otherwise, numerical results are presented in atomic units (a.u.), i.e., we set $\hbar = |e| = m_e = 1$. However, in our derivations we keep the electron mass (m_e) and charge ($e < 0$) explicitly. Our results are shown in terms of the atomic units of momentum, $p_{at} = \alpha m_e c$, and electric field, $\mathcal{E}_{at} = \alpha^2 m_e c^2/(|e|a_0)$, where α is the fine-structure constant, c is the speed of light (equal to $1/\alpha$ in a.u.), and a_0 is the Bohr radius.

II. ELECTRON VORTEX STRUCTURES

We start by analyzing a general electron wave function $\psi(\boldsymbol{r})$ in the configuration space. The concepts of *nodes* and *vortices* are related, as both are zeros of the complex wave function $\psi(\boldsymbol{r})$ [meaning that the real and imaginary parts of $\psi(\boldsymbol{r})$ vanish at those points]. They can form, in general, various geometrical structures such as isolated points, curves, or surfaces which may intersect with each other. In particular, if we restrict our analysis to a two-dimensional (2D) plane (denoted below by Π) in the three-dimensional configuration space, the zeros of the wave function appear on that plane as curves or individual points. Now, in order to distinguish between nodes and vortices, we define the velocity distribution

$$\boldsymbol{v}(\boldsymbol{r}) = \frac{1}{m_e}\frac{\mathrm{Re}\,[\psi^*(\boldsymbol{r})(-i\nabla)\psi(\boldsymbol{r})]}{|\psi(\boldsymbol{r})|^2}, \tag{1}$$

and project it onto the plane Π. If the plane is perpendicular to the unit vector $\boldsymbol{N}$, i.e., it is defined by the equation

$$\Pi: \quad \boldsymbol{N}\cdot\boldsymbol{r} - d = 0, \tag{2}$$

with d being an arbitrary real number, then the longitudinal velocity distribution is

$$\boldsymbol{v}_\parallel(\boldsymbol{r}) = \boldsymbol{v}(\boldsymbol{r}) - [\boldsymbol{v}(\boldsymbol{r})\cdot\boldsymbol{N}]\boldsymbol{N}, \tag{3}$$

where $\boldsymbol{r}$ satisfies Eq. (2). Furthermore, the circulation of the velocity distribution (3) is quantized. Namely, in the absence of a magnetic field,

$$\oint_K m_e \boldsymbol{v}_\parallel(\boldsymbol{r})\cdot d\boldsymbol{r} = 2\pi m, \tag{4}$$

where $m = \pm 1, \pm 2, \ldots$ for a vortex and $m = 0$ for a node. Here K denotes a closed path (oriented counterclockwise) in the plane (2) and m is the so-called *topological charge* or *winding number* [18–20]. So the node can be regarded as a special case of the vortex with zero strength (topological charge) [21]. For simplicity, in the remaining part of the paper, the vortex is referred to as a nonvanishing topological charge vortex. The points belonging to the path K can be parametrized as a function $\boldsymbol{r}(u)$, with $0 \leqslant u \leqslant u_0$. However, as the curve K is closed, the condition $\boldsymbol{r}(0) = \boldsymbol{r}(u_0)$ must be satisfied.

To proceed with our analysis, we represent the complex wave function $\psi(\boldsymbol{r})$ in terms of two real functions $R(\boldsymbol{r})$ and $S(\boldsymbol{r})$,

$$\psi(\boldsymbol{r}) = R(\boldsymbol{r})e^{iS(\boldsymbol{r})}. \tag{5}$$

Clearly, the phase of the wave function $S(\boldsymbol{r}) = \arg[\psi(\boldsymbol{r})] \bmod 2\pi$ is not uniquely defined. However, as was pointed out by Dirac [22], in order to ensure that the wave function is single valued, the condition

$$\oint_K \nabla S(\boldsymbol{r})\cdot d\boldsymbol{r} = 2\pi m, \quad m = 0, \pm 1, \pm 2, \ldots \tag{6}$$

must hold. Hence, by circulating around the vortex, the phase of the wave function changes continuously between S_0 and $S_0 + 2\pi m$ ($m \neq 0$). This is not the case for the nodes. In most cases, the latter form curves and $S(\boldsymbol{r})$ jumps across them by π, meaning that $S(\boldsymbol{r}) = S_0$ or $S(\boldsymbol{r}) = S_0 + \pi$ around a standard node. It may also happen that the nodal curve is tangent to the plane Π. In this case, we will observe an isolated zero for which, in the close vicinity, the phase of the wave function takes nearly the same values. As a result, the circulation of $\nabla S(\boldsymbol{r})$ along a closed contour encircling the nodes is zero ($m = 0$).

In closing this section, a couple of remarks should be made. First of all, Eq. (4) is typically written in terms of the field $\boldsymbol{v}(\boldsymbol{r})$ rather than $\boldsymbol{v}_\parallel(\boldsymbol{r})$ (see, for instance, [18–20]). The point is, however, that the circulation of the normal component of $\boldsymbol{v}(\boldsymbol{r})$ along the contour K is identically equal to zero. This leaves us with Eq. (4). Second of all, it follows from Eqs. (1) and (5) that $m_e\boldsymbol{v}(\boldsymbol{r}) = \nabla S(\boldsymbol{r})$. It is not surprising therefore that

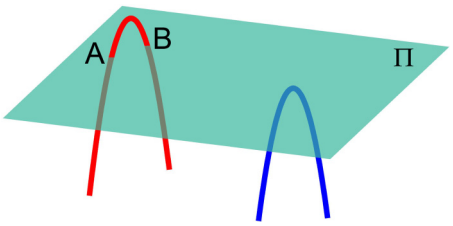

FIG. 1. Situations which may lead to misinterpretation of numerical results. (a) The vortex curve intersects twice the plane Π at points A and B, which are very close to each other (red curve). The circulation around a closed loop enclosing them will identify the two vortices as a single nonvortex node. (b) The vortex curve comes very close to the plane Π. However, it does not cross it (blue curve). The numerical analysis identifies a nonvortex nodal point. In order to obtain a proper interpretation, it becomes necessary to redefine the velocity field $\boldsymbol{v}_{\parallel}(\boldsymbol{r})$ by shifting or rotating the plane defined by Eq. (2).

the conditions (4) and (6) are equivalent, and both can be used to determine the topological charge m. Finally, we stress that vortices are determined numerically, i.e., with a finite resolution. This could lead to misinterpretation of numerical results. For instance, one could meet the situations illustrated in Fig. 1. The red curve here intersects the plane Π at two points, A and B. If such points are close enough (i.e., the distance between them is similar or smaller than the numerical accuracy) one cannot recognize them as individual vortices. This is due to the fact that the circulation around a contour K, surrounding both of them, vanishes. It may also happen that the vortex curve approaches the plane very closely but it does not intersect it (blue curve). In this case the circulation vanishes as well. One can see that in both cases the numerical analysis would fail in determining the vortex character of the curve. If this happens, it is necessary to select another plane and analyze a new vector field (3) in the vicinity of the curve. The point is that the strength of the vortex defined by the value of m is independent of that choice.

The discussion above concerns the wave function in the configuration space. However, as proposed by Berry [23], it can be generalized to an arbitrary complex function $f(\boldsymbol{R})$ depending on three real parameters $\boldsymbol{R} = (R_x, R_y, R_z)$. For the function $f(\boldsymbol{R})$ and the parametric space $\boldsymbol{R}$, we shall choose the probability amplitude of photodetachment $\mathcal{A}(\boldsymbol{p})$ and the momentum space $\boldsymbol{p}$, respectively. This will allow us to investigate the nodes and vortex structures in photodetachment, as introduced in the next section.

III. PROBABILITY AMPLITUDE OF DETACHMENT AND FORMATION OF VORTEX STRUCTURES

In this paper, we analyze the photodetachment from H^- under the scope of the SFA [15,24]. The interaction between the active electron and neutral core is modeled as a zero-range potential (ZRP). The bound state wave function for the ZRP (s states) is given by [15,24]

$$\Phi_s(\boldsymbol{r}) = \langle \boldsymbol{r}|\Phi_s\rangle \approx \frac{1}{\sqrt{4\pi}}\frac{A}{r}e^{-\kappa r}, \tag{7}$$

where A and κ are constant. While κ determines the bound-state energy $E_0 = -(\alpha c)^2 m_e \kappa^2/2$, A is a fitting parameter that can be adjusted such that the detachment probabilities are consistent with either experimental results or with the *ab initio* TDSE calculations. In our analysis we use the values $\kappa = 0.2354$ a.u. and $A = 0.75$ a.u., following Ref. [24]. We consider detachment by a single ultrashort laser pulse of circular polarization, or by two such pulses in the corotating or counter-rotating configurations. The laser field is treated in the dipole approximation, i.e., we use a time-dependent vector potential $\boldsymbol{A}(t)$ to define our field. Furthermore, we impose the conditions $\boldsymbol{A}(t < 0) = \boldsymbol{A}(t > T_p) = \boldsymbol{0}$ for a finite pulse or train of pulses. Here T_p defines the full duration of the single or double pulse.

In this section, we present the probability amplitude of photodetachment $\mathcal{A}(\boldsymbol{p})$ calculated in the SFA in the length gauge (for more details on the derivations we refer the reader to Ref. [15]). Even though the SFA leads to gauge-invariant results when the unperturbed electron ground state is given by Eq. (7), the length gauge seems to be favorable as it requires less computational effort. For this reason, this is our choice of gauge and we shall use the following expression for the probability amplitude [15]:

$$\mathcal{A}(\boldsymbol{p}) = -i\int_0^{T_p} dt\, \langle \psi_{\boldsymbol{p}}(t)|\hat{H}_I(t)|\Phi_s(t)\rangle. \tag{8}$$

Here, $|\psi_{\boldsymbol{p}}(t)\rangle$ represents the Volkov solution [25] of the electron in the laser field whereas $\hat{H}_I(t)$ is the interaction Hamiltonian, both in the length gauge. The latter is given by

$$\hat{H}_I(t) = -e\boldsymbol{\mathcal{E}}(t)\cdot\boldsymbol{r}, \tag{9}$$

where $\boldsymbol{\mathcal{E}}(t) = -\partial_t \boldsymbol{A}(t)$ is the electric field defining the laser pulse. Furthermore, $|\Phi_s(t)\rangle$ is the unperturbed ground-state wave function of the negative ion such that $\langle \boldsymbol{r}|\Phi_s(t)\rangle = \Phi_s(\boldsymbol{r})e^{-iE_0 t}$, where E_0 is the bound-state energy ($|E_0| = 0.754$ eV) and $\Phi_s(\boldsymbol{r})$ is given by Eq. (7). By introducing the corresponding Volkov solution, we arrive at the following expression for the probability amplitude:

$$\mathcal{A}(\boldsymbol{p}) = ie\int_0^{T_p} dt\, \boldsymbol{\mathcal{E}}(t)\cdot\tilde{\boldsymbol{\Phi}}_s[\boldsymbol{p} - e\boldsymbol{A}(t)]\exp\left(i\left[\frac{\boldsymbol{p}^2}{2m_e} - E_0\right]t - \frac{i}{m_e}\int_0^t dt'\left[e\boldsymbol{A}(t')\cdot\boldsymbol{p} - \frac{e^2\boldsymbol{A}^2(t')}{2}\right]\right), \tag{10}$$

where we have introduced the function

$$\tilde{\boldsymbol{\Phi}}_s(\boldsymbol{p}) = i\nabla_{\boldsymbol{p}}\tilde{\Phi}_s(\boldsymbol{p}) = -i\frac{4\sqrt{\pi}A}{(\kappa^2 + \boldsymbol{p}^2)^2}\boldsymbol{p}, \tag{11}$$

and $\tilde{\Phi}_s(\boldsymbol{p})$ is the Fourier transform of Eq. (7). In contrast to Ref. [24], where the saddle-point method is used to approximate the time integral in Eq. (10), we calculate it numerically.

Once the amplitude $\mathcal{A}(\boldsymbol{p})$ is obtained from Eqs. (11) and (10), one can determine the probability distribution of photodetachment [15],

$$\bar{\mathcal{P}}(\boldsymbol{p}) = \frac{1}{(2\pi)^3}|\mathcal{A}(\boldsymbol{p})|^2. \tag{12}$$

This will be done in Sec. IV for three different configurations of the driving field (see below).

For the numerical solution of the TDSE, we consider the electron wave function $\psi(\boldsymbol{r},t)$ interacting with both the laser field and a Yukawa potential of the form

$$V(r) = -1.1\alpha c\frac{e^{-r/a_0}}{r}. \tag{13}$$

Note that the parameters used to define our short-range potential are such that the electron affinity of the negative ion is the same in both SFA and TDSE. The Hamiltonian, which governs the temporal evolution of the electron, is therefore given by

$$H(t) = -\frac{\boldsymbol{\nabla}^2}{2m_\mathrm{e}} + V(r) + i\frac{e}{m_\mathrm{e}}\boldsymbol{A}(t)\cdot\boldsymbol{\nabla}, \tag{14}$$

where higher order terms in the vector potential are neglected. As one can see, we use our Hamiltonian in the velocity gauge, as our method to solve TDSE is gauge invariant.

By expanding the electron wave function in spherical harmonics and projecting the final state onto the scattering state of the pure Yukawa potential (13), we find out that the probability amplitude of detachment takes the form

$$\mathcal{A}(\boldsymbol{p}) = \frac{2\pi}{p}\sum_{l,m}(-i)^l e^{i\delta_l}Y_{lm}(\hat{\boldsymbol{p}}) \times \int_0^{r_\mathrm{max}} dr\,\psi_{lm}(r,t_f)rR_{pl}(r). \tag{15}$$

Here, $\hat{\boldsymbol{p}} = \boldsymbol{p}/p$ defines the polar and azimuthal angles of the electron momentum, R_{pl} is the radial part of the scattering state, and δ_l is the phase shift. Furthermore, t_f is the final time of propagation and $\psi_{lm}(r,t)$ are the components defining the expansion of $\psi(\boldsymbol{r},t)$ in the spherical harmonics $Y_{lm}(\hat{\boldsymbol{r}})$. In other words, $\psi_{lm}(r,t)$ are such that

$$\psi(\boldsymbol{r},t) = \frac{1}{r}\sum_{l=0}^{l_\mathrm{max}}\sum_{m=-l}^{l}\psi_{lm}(r,t)Y_{lm}(\hat{\boldsymbol{r}}), \tag{16}$$

with $\hat{\boldsymbol{r}} = \boldsymbol{r}/r$. For numerical methods, we use the finite difference method to discretize the radial coordinate r and the Cranck-Nicholson propagator to determine the evolution of the electron from the initial to the final state.

A. Circulation and topological charge

Before defining the driving field used in our numerical illustrations, we describe here how to calculate the topological charge around a closed loop K in a 2D plane. In momentum space, the topological charge is [cf. Eq. (4)]

$$m = \frac{1}{2\pi}\oint_K \boldsymbol{v}(\boldsymbol{p})\cdot d\boldsymbol{p}, \tag{17}$$

where $\boldsymbol{v}(\boldsymbol{p})$ is an analog to the velocity field (1). It is now defined as

$$\boldsymbol{v}(\boldsymbol{p}) = \frac{1}{|\mathcal{A}(\boldsymbol{p})|^2}\mathrm{Re}\,[\mathcal{A}^*(\boldsymbol{p})(-i\boldsymbol{\nabla}_{\boldsymbol{p}})\mathcal{A}(\boldsymbol{p})], \tag{18}$$

where $\mathcal{A}(\boldsymbol{p})$ is the complex probability amplitude (10) and $\boldsymbol{\nabla}_{\boldsymbol{p}}$ is the gradient calculated with respect to the momentum coordinates. To parametrize the path K, we consider a circular contour of radius p_r centered at $\boldsymbol{p} = \boldsymbol{0}$, namely, we choose

$$K: \quad p_x^2 + p_y^2 = p_r^2; \quad p_z = 0. \tag{19}$$

Therefore, it becomes natural to introduce the polar coordinates (p_r,φ) such that

$$p_x = p_r\cos\varphi, \quad p_y = p_r\sin\varphi, \quad p_z = 0. \tag{20}$$

Hence, the probability amplitude becomes also a function of those variables, i.e., $\mathcal{A}(p_r,\varphi) \equiv \mathcal{A}(p_r\cos\varphi, p_r\sin\varphi, 0)$. It follows from Eq. (17) that the topological charge $m \equiv m(p_r)$ is given by

$$m(p_r) = \frac{1}{2\pi}\int_0^{2\pi} p_r\boldsymbol{v}(\boldsymbol{p})\cdot\boldsymbol{e}_\varphi d\varphi = \frac{1}{2\pi}\int_0^{2\pi} p_r v_\parallel(p_r,\varphi)d\varphi, \tag{21}$$

where

$$p_r v_\parallel(p_r,\varphi) = \frac{1}{|\mathcal{A}(p_r,\varphi)|^2}\mathrm{Im}\,[\mathcal{A}^*(p_r,\varphi)\partial_\varphi\mathcal{A}(p_r,\varphi)], \tag{22}$$

and $\boldsymbol{e}_\varphi$ is the angular unit vector. It should acquire integer values forming a "staircase" plot as a function of p_r and it provides information about the number of vortex points surrounded by the closed path. This will be illustrated in Sec. IV B.

The probability amplitudes in quantum mechanics are defined up to a global phase. It means that we can redefine the probability amplitude of photodetachment such that $\mathcal{A}'(\boldsymbol{p}) = \exp[i\Lambda(\boldsymbol{p})]\mathcal{A}(\boldsymbol{p})$, where $\Lambda(\boldsymbol{p})$ is an arbitrary continuous phase. Although the "velocity" (in the momentum space) $\boldsymbol{v}(\boldsymbol{p})$ introduced above (which is related to the Berry connection [23]) is gauge dependent, the topological charges are independent of a chosen phase $\Lambda(\boldsymbol{p})$. The same concerns nodal surfaces and vortex curves, as the phase factor $\exp[i\Lambda(\boldsymbol{p})]$ never vanishes.

B. Laser field

In our numerical calculations, we shall use a circularly polarized laser pulse (or train of such pulses) propagating along the $\boldsymbol{e}_z$ axis. The polarization plane, therefore, is the xy plane. Each individual pulse consists of $N_\mathrm{osc} = 3$ field oscillations within a sine-squared envelope. The integer $N_\mathrm{rep} = 1, 2$ determines the number of pulses and δ defines its polarization ($\delta = \pm\pi/4$ for circularly polarized fields) [see Eqs. (24) and (25) below]. With this in mind, we define the electric field as follows:

$$\boldsymbol{\mathcal{E}}(\phi) = \mathcal{E}_\mathrm{at}\sqrt{\frac{I}{I_\mathrm{at}}}[F_1(\phi)\boldsymbol{e}_x + F_2(\phi)\boldsymbol{e}_y]. \tag{23}$$

Here $I_\mathrm{at} = 3.51\times10^{16}$ W/cm^2 is the atomic unit of intensity, I is the intensity of the light field, $\phi = \omega t$ is its phase, and $\omega = 2\pi/T_p$. Furthermore, the laser carrier frequency is $\omega_\mathrm{L} = \omega N_\mathrm{osc}N_\mathrm{rep}$ which corresponds to the wavelength $\lambda_\mathrm{L} = 2\pi c/\omega_\mathrm{L}$. In Eq. (23), we have introduced the electric field shape functions, $F_j(\phi)$, $j = 1, 2$, which are given by

$$F_1(\phi) = \left[\sin\left(\frac{N_\mathrm{rep}\phi}{2}\right)\right]^2\sin(N_\mathrm{rep}N_\mathrm{osc}\phi)\cos(\delta), \tag{24}$$

$$F_2(\phi) = -\left[\sin\left(\frac{N_\mathrm{rep}\phi}{2}\right)\right]^2\cos(N_\mathrm{rep}N_\mathrm{osc}\phi)\sin(\delta), \tag{25}$$

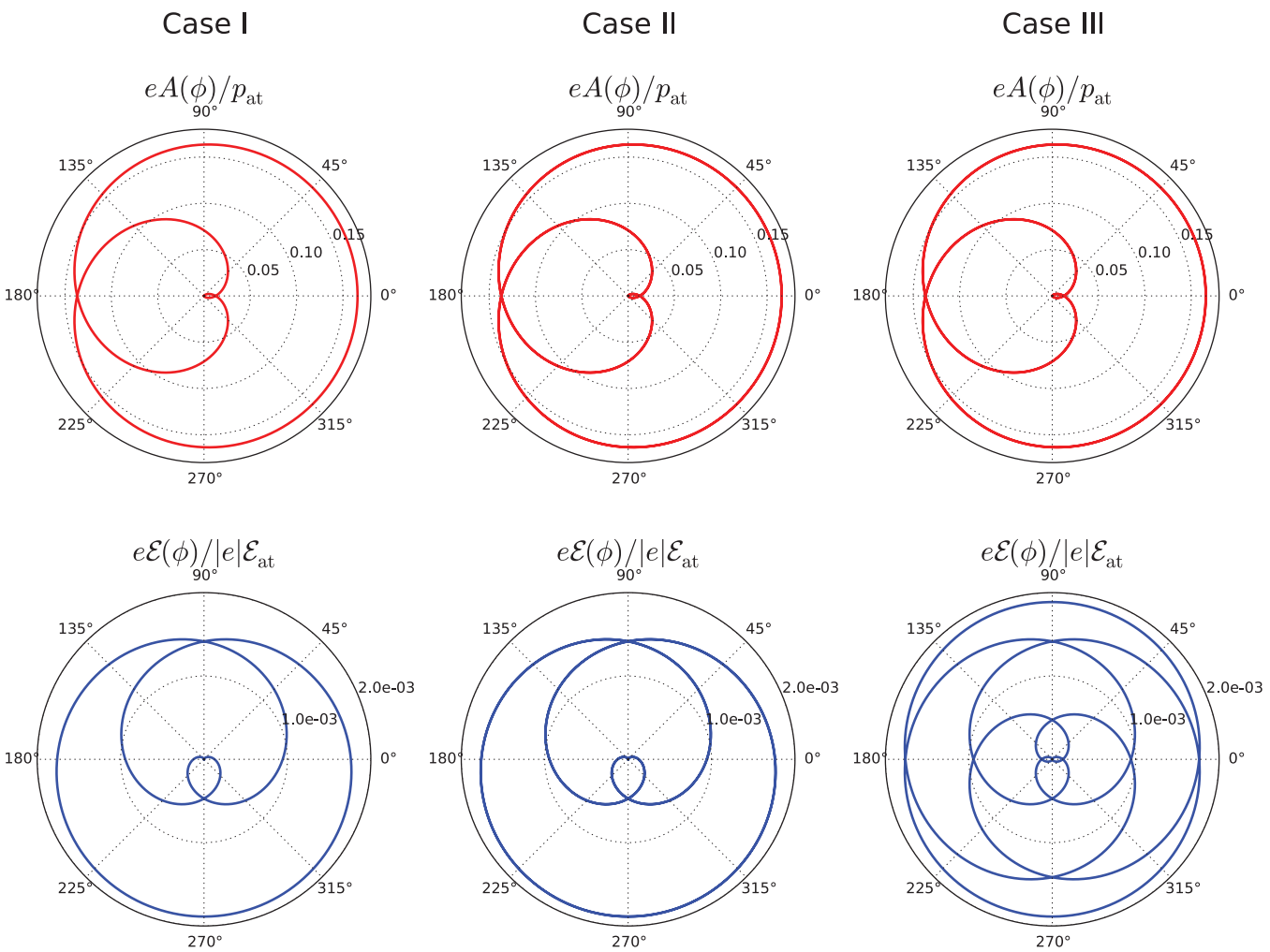

FIG. 2. Parametric plots of the vector potential $\boldsymbol{A}(\phi)$ [Eq. (26)] (upper row) and electric field $\boldsymbol{\mathcal{E}}(\phi)$ [Eqs. (23)–(25)] (lower row) for three types of driving fields used in this paper. In all cases the intensity is $I = 2.5 \times 10^{11}$ W/cm^2, each individual pulse comprises three oscillations ($N_{\rm osc} = 3$), and the laser field wavelength is $\lambda_{\rm L} = 4000$ nm. While case I (left column) illustrates the properties of a single light pulse ($N_{\rm rep} = 1$) of circular polarization ($\delta = \pi/4$), case II (middle column) and case III (right column) relate to trains of two pulses ($N_{\rm rep} = 2$) with corotating ($\delta = \pi/4$) and counter-rotating ($\delta = \pi/4$ for $\phi \in [0, \pi]$ and $\delta = -\pi/4$ for $\phi \in [\pi, 2\pi]$) polarizations, respectively.

for $\phi \in [0, 2\pi]$ and zero otherwise. In numerical calculations, we shall use $I = 2.5 \times 10^{11}$ W/cm^2 and $\lambda_{\rm L} = 4000$ nm. Note that, for $N_{\rm rep} > 1$ we can change the polarization phase from pulse to pulse. Our aim in this paper is to compare the photoelectron probability distribution of detachment for three cases of the driving field: single laser pulse ($N_{\rm rep} = 1$, $\delta = \pi/4$), two corotating ($N_{\rm rep} = 2$, $\delta = \pi/4$), and counter-rotating identical pulses ($N_{\rm rep} = 2$, $\delta = \pi/4$ for $t \leqslant T_p/2$ and $\delta = -\pi/4$ for $t > T_p/2$). We label those three cases as case I, case II, and case III, respectively. In case II and case III, we keep $N_{\rm osc} = 3$ and $\lambda_{\rm L} = 4000$ nm unchanged. So ω in these two cases changes, i.e., the pulse duration T_p doubles. Basically, in case II, we have two identical pulses of case I sequentially. In case III, we have the same pulse of case I and another counter-rotating pulse sequentially.

Finally, the vector potential describing the driving field is given by

$$\boldsymbol{A}(\phi) = -\frac{1}{\omega}\int_0^{\phi} \boldsymbol{\mathcal{E}}(\phi')d\phi', \tag{26}$$

and, for our current parameters, we have that

$$\int_0^{2\pi} F_j(\phi')d\phi' = 0, \quad j = 1, 2. \tag{27}$$

This ensures that $\boldsymbol{A}(0) = \boldsymbol{A}(2\pi) = \boldsymbol{0}$, i.e., the vector potential vanishes for $t < 0$ and $t > T_p$.

In Fig. 2, we show the temporal evolution of the tips of the vector potential (upper row) and electric field (lower row) for the driving fields in case I (left column), case II (middle column), and case III (right column). All curves, which are generated by changing the phase ϕ from 0 to 2π, start and end at the origin of coordinates. While in case I both $\boldsymbol{A}(\phi)$ and $\boldsymbol{\mathcal{E}}(\phi)$ evolve counterclockwise by making one complete turn around the spiral, in case II the fields complete two turns in the same direction. In case III the vector potential evolves counterclockwise for $0 \leqslant \phi \leqslant \pi$ and clockwise for $\pi < \phi \leqslant 2\pi$ by following the same path; however, the electric field not only changes its direction but also follows a different path (see the lower-right panel), such that the symmetry up-down

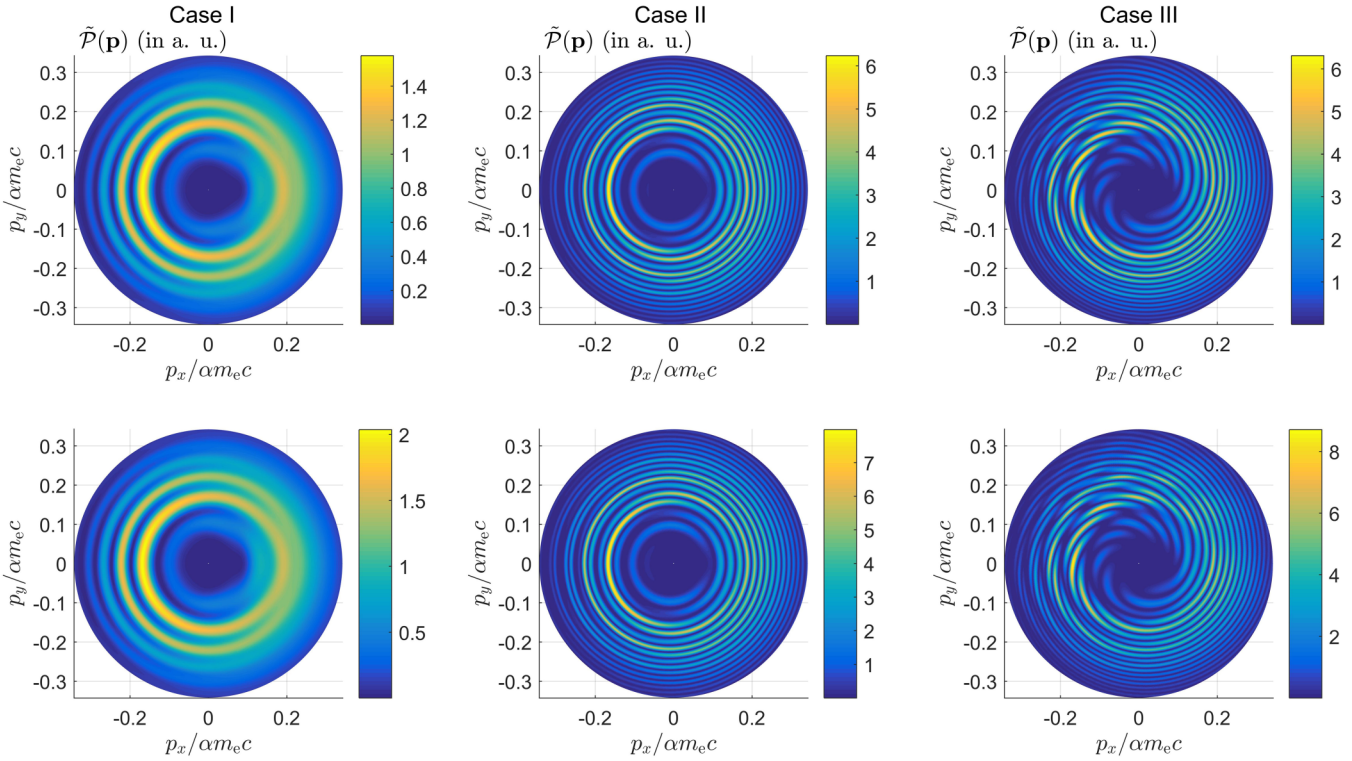

FIG. 3. Color maps of the probability distributions $\tilde{\mathcal{P}}(\boldsymbol{p})$ [Eq. (12)] in the $p_x p_y$ plane ($p_z = 0$) calculated from the SFA [Eq. (10)] (upper row) and the numerical solution of the TDSE (lower row), in atomic units. While the left column concerns case I, the middle and right columns are for cases II and III, respectively (see Fig. 2). Both momentum distributions from the two methods exhibit very similar structures and differ approximately by a scaling factor equal to 4/3, that can be incorporated into the SFA by multiplying the parameter A in (7) by around 1.15.

is preserved. In consequence, the momentum probability distribution also acquires this property.

IV. PROBABILITY DISTRIBUTION OF PHOTOELECTRONS IN THE MOMENTUM SPACE

In this section, we present the probability distribution of electrons $\tilde{\mathcal{P}}(\boldsymbol{p})$ [Eq. (12)] in photodetachment driven by laser fields in three cases described in Fig. 2. In Fig. 3, we show such distributions obtained from SFA [Eq. (10)] (upper row) and by solving the TDSE (lower row) for case I (left column), case II (middle column), and case III (right column). Our results are presented in the $p_x p_y$ plane, namely, $\tilde{\mathcal{P}}(\boldsymbol{p})$ is calculated for $p_z = 0$. By comparing the upper and lower rows, we see that the SFA leads to accurate qualitative results. The difference is in a common scaling factor. By multiplying the SFA distributions by a factor of roughly 4/3 we obtain a very good quantitative comparison. Note that this factor can be assimilated into the parameter A in Eq. (7). Such a good agreement between both treatments is expected due to the absence of a Coulomb interaction with the parent atom when the electron is in the continuum. However, the SFA presents several advantages over the solution of the TDSE, including the simplicity of numerical calculations together with a larger accuracy (i.e., fine details can be better displayed), and the possibility to analyze photodetachment in a broader range of field intensities and frequencies. This is provided that the total probability of detachment, as computed from our method, is always smaller than 1 (for restrictions of our model, we refer the reader to Ref. [15]). Such condition is fulfilled for all calculations presented in this paper. Consider the probability distribution $\tilde{\mathcal{P}}(\boldsymbol{p})$ [Eq. (12)] for case I (left column of Fig. 3). This distribution is characterized by strong interference effects where regions of high probability appear as concentric rings separated by annular zones of low probability (in the terminology coined in Ref. [4], those rings correspond to *zero-start* spirals). This is particularly visible in the negative part of the p_x axis. Nevertheless, in the positive p_x axis some of the rings seem to partially merge together in order to produce a modulated electron supercontinuum [15,26–28]. As one of the conditions for the generation of vortices is the vanishing of the wave function, for $|\boldsymbol{p}|/p_{\text{at}} > 0.1$, we expect to find them in the negative part of the p_x axis. This is because the rings do not merge there, and deep minima between zones of high probability are observed.

For a laser field consisting of two corotating light pulses (case II, middle column of Fig. 3), the interference effects are more pronounced as compared to case I. Namely, we observe many more large-probability rings which are fully separated at all angles $\varphi_{\boldsymbol{p}}$, i.e., no supercontinuum is formed. In contrast, the counter-rotating configuration (case III, right column of the same figure) leads to a completely different pattern, in which case multiarm spiral-like structures, similar to what was predicted in, e.g., Refs. [1,4], dominate the probability distribution and no concentric rings can be distinguished.

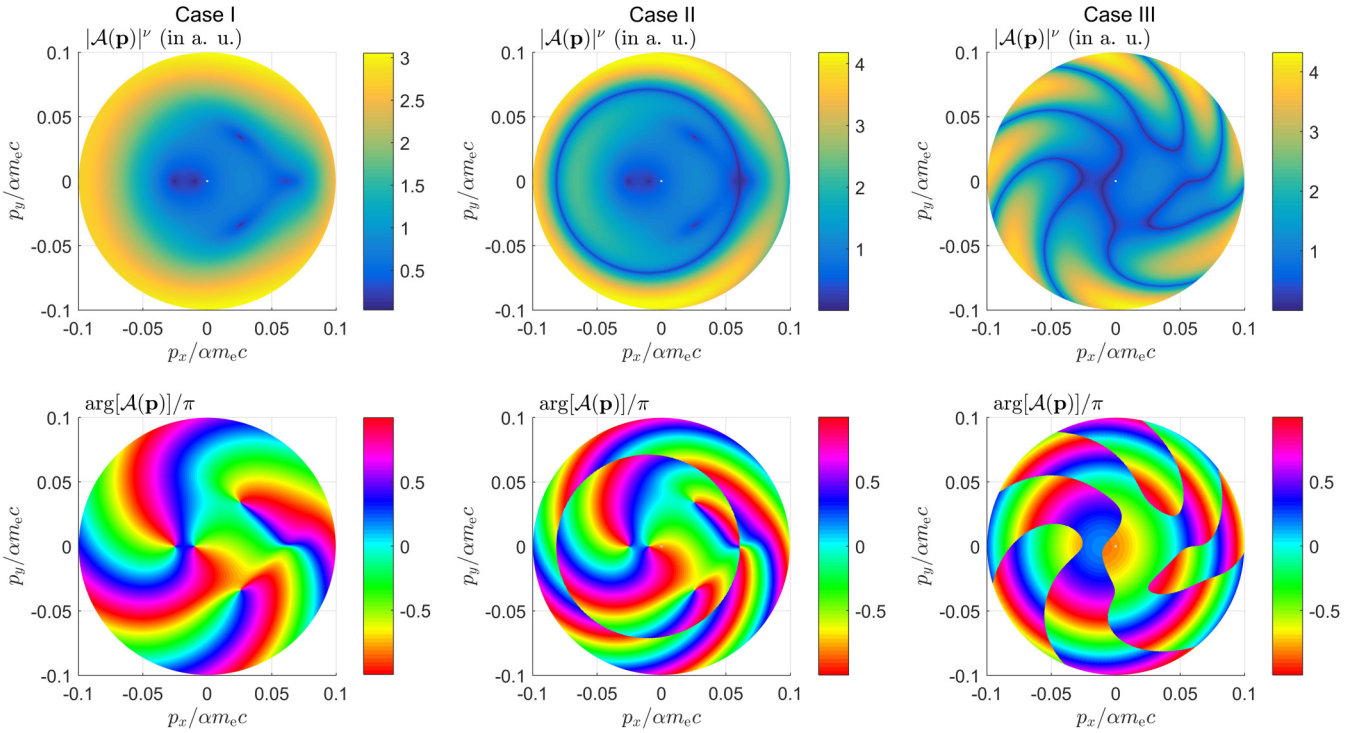

FIG. 4. Magnitude (upper row) and phase (lower row) of the probability amplitude $\mathcal{A}(\boldsymbol{p})$ calculated from the SFA formalism [Eq. (10)] in the $p_x p_y$ plane ($p_z = 0$). While the left column corresponds to case I, the middle and right columns correspond to case II and case III, respectively [see Fig. (2)]. The magnitude of probability amplitudes is raised to the power $\nu = 0.5$ in order to better display details of the vortex structures and nodal lines.

A. Phase and magnitude of the probability amplitude

It follows from Sec. II that the probability amplitude vanishes at the photoelectron momenta that correspond to either vortices or nodes. To distinguish between them, it is necessary to analyze the behavior of the amplitude's phase in the vicinity of those points. If the phase varies continuously between 0 and an integer multiple of 2π by following a closed path around the zero of $\mathcal{A}(\boldsymbol{p})$, we have a vortex. In contrast, if the phase remains approximately constant or jumps by π, we have a zero-strength vortex. Hence, in order to determine whether or not vortices are formed during photodetachment, we analyze separately the phase, $S_{\mathcal{A}}(\boldsymbol{p}) = \arg[\mathcal{A}(\boldsymbol{p})] \bmod 2\pi$, and magnitude, $|\mathcal{A}(\boldsymbol{p})|$, of the probability amplitude in the SFA [Eq. (10)]. This is shown in Fig. 4 for case I (left column), case II (middle column), and case III (right column). For the sake of comparison, in Fig. 5 we show the same but obtained from the numerical solution of the TDSE. By comparing Figs. 4 and 5 we see that the strong-field approximation gives similar results as compared to those of TDSE; however, there are some differences. The main difference between those two figures is for case III (right columns) at low photoelectron momenta ($-0.05\alpha m_e c < p_x < 0$ and $p_y \approx 0$). While the SFA predicts there the formation of two separated nodal surfaces, the TDSE shows that both of them merge or approach each other very closely. Nevertheless, no vortices are formed (see the lower-right panel of Fig. 5). The magnitude and phase of the probability amplitude obtained from both treatments are very similar in the remaining regions of momentum space, except of case I (upper-left and lower-left panels of the same figures). The SFA locates a local minimum (but not a node) on the right-hand side of the plots; however, the TDSE identifies there a vortex-antivortex pair. This will be analyzed below.

First, we consider case I calculated by solving numerically the TDSE (left column of Fig. 5). It seems that the probability amplitude vanishes at six different points for the momentum range considered here ($|\boldsymbol{p}|/\alpha m_e c < 0.1$). One pair of them, located at $p_x < 0$ is rather difficult to resolve. The interpretation of such a structure as either two separate vortices or as a single broad local minimum (both shown in Fig. 1) is not possible. This is due to the lower resolution of the TDSE (as compared to SFA) and the inherent computational difficulties while solving it. However, the remaining four points of vanishing probability are well resolved and, from the amplitude's phase, one can recognize that these are vortices. In particular, at the right portion of the plots we observe the formation of a vortex-antivortex pair located close to each other. This corresponds to the situation illustrated by the red curve in Fig. 1.

When the SFA is used for case I (left column of Fig. 4), the low-energy structure ($p_x < 0$) can be better resolved than in Fig. 5. This time, we observe the formation of two well-defined vortices with topological charges $m = 1$. In contrast to the TDSE, the rightmost vortex-antivortex pair appears here as a single local minimum, which corresponds to the blue curve in Fig. 1. This, in turn means that, while the SFA predicts a vortex curve which approaches closely the $p_x p_y$ plane and turns around before crossing it, the TDSE predicts that such curve comes back shortly after traversing that plane. For this reason, two vortices with opposite winding numbers

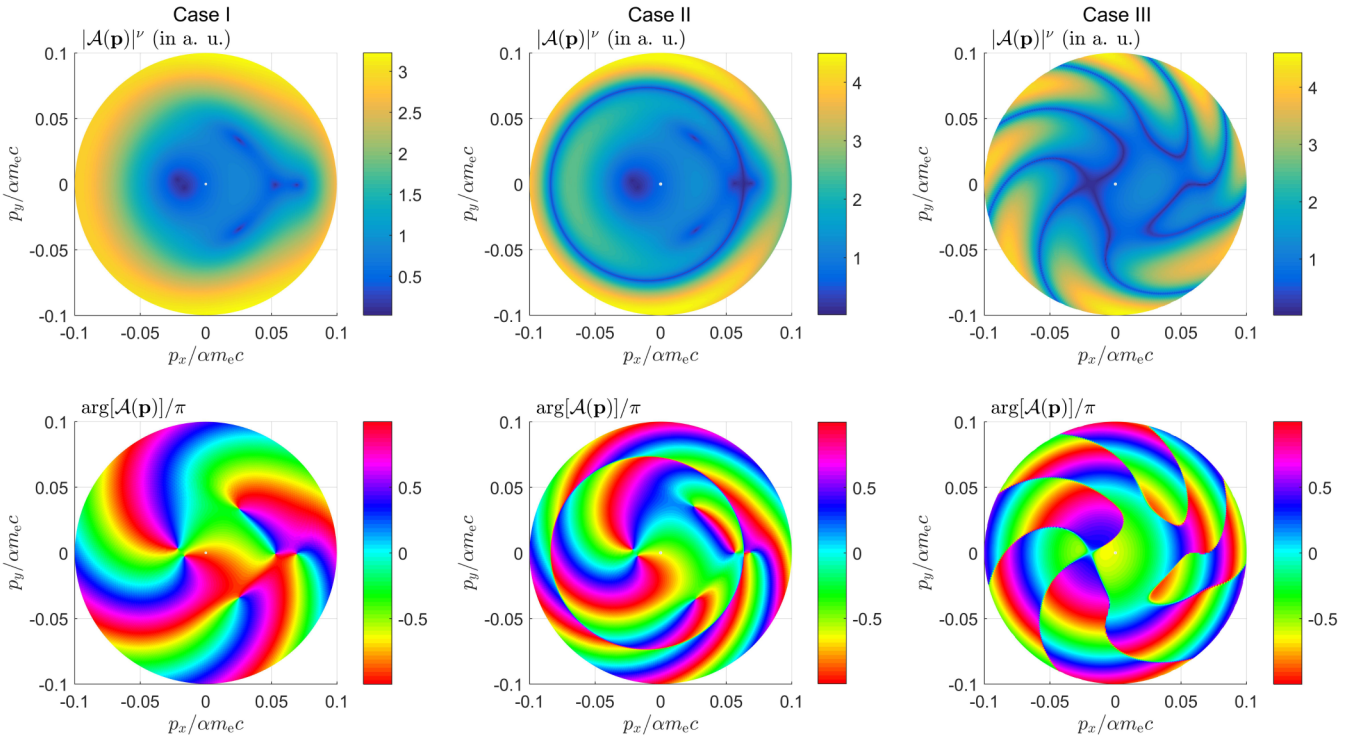

FIG. 5. The same as those in Fig. 4 but calculated from the numerical solution of the TDSE.

are observed in the TDSE instead of one local minimum as in the SFA.

For a driving field consisting of two corotating pulses (case II), the same vortices and points of small probability as in case I are observed. This is true for both SFA and TDSE by comparing the left and middle panels of Figs. 4 and 5 independently. However, in each case an additional nodal ring appears. The concentric rings are nonvortex nodal curves as, by crossing them, the phase of $\mathcal{A}(\boldsymbol{p})$ changes abruptly by π. This indicates that vortex structures in the probability amplitude of detachment are created by a single pulse. The train of identical pulses does not affect the vortex pattern, but only adds extra nonvortex nodal lines into the distribution.

Finally, the counter-rotating configuration (case III) leads to spiral-like nonvortex curves, as shown in the right columns of Figs. 4 and 5. Hence, we stress that helixlike structures in the probability distribution of photoelectrons *are not* related to vortices.

In summary, after analyzing the phase and magnitude of the probability amplitude of photodetachment in the given plane of momentum space, we conclude that single and double corotating laser pulses lead to the generation of vortex structures in photodetachment with topological charges $m = \pm 1$. However, two counter-rotating pulses create spiral-like structures which do not have vortex character. This will be further analyzed in the next section.

B. Topological charge in photodetachment

In Sec. III A, we have defined the circulation and the topological charge of photoelectrons in the momentum space. Here we shall relate to those concepts. As we have shown above, both SFA and TDSE lead to similar probability amplitudes (phase and magnitude), for the laser parameters considered in this paper. Thus in the following we shall present the results from the SFA only.

In the lower row of Fig. 6, we plot $p_r v_{\parallel}(p_r, \varphi)$ [Eq. (22)] as a function of the azimuthal angle φ (p_r has been fixed to $0.2\alpha m_e c$ in each panel). In the upper row, we show the winding numbers $m(p_r)$ calculated from (21) for different closed paths, as defined by the parametrization (20). Our results are shown for case I (left column), case II (middle column), and case III (right column). The main conclusions from this figure stem from the behavior of the topological charges; it can be seen that, for a single pulse and for two pulses with corotating polarizations (cases I and II, respectively), $m(p_r)$ acquires integer values while forming a staircase structure as a function of p_r. The increments in the winding number happen when the integration contour encircles new vortex points [22]. However, a close inspection of the topological charges reveals points with noninteger values. This anomaly appears when the path K goes across (or passes very close to) a vortex structure; as the probability amplitude vanishes there, both $\boldsymbol{v}(\boldsymbol{p})$ [Eq. (18)] and the line integral are not accurately evaluated which, in turn, creates numerical errors in the determination of $m(p_r)$ [Eq. (21)]. For $p_r > 0.1\alpha m_e c$, we observe the systematic increase of $m(p_r)$ by 1. This is due to the fact that for such momenta the vortices are located only on the negative p_x axis, where even for a single pulse the strong diffraction-interference pattern is detected.

Let us go back to case III. From the upper-right panel of Fig. 6, we see that $m(p_r)$ is always zero. This means that no vortices are enclosed by the circular path K, independently of its radius p_r. Furthermore, the quantity $p_r v_{\parallel}(p_r, \varphi)$ shown in the lower-right panel of Fig. 6 behaves similarly to a negative sinusoidal function of φ (p_r constant). Hence, its integral

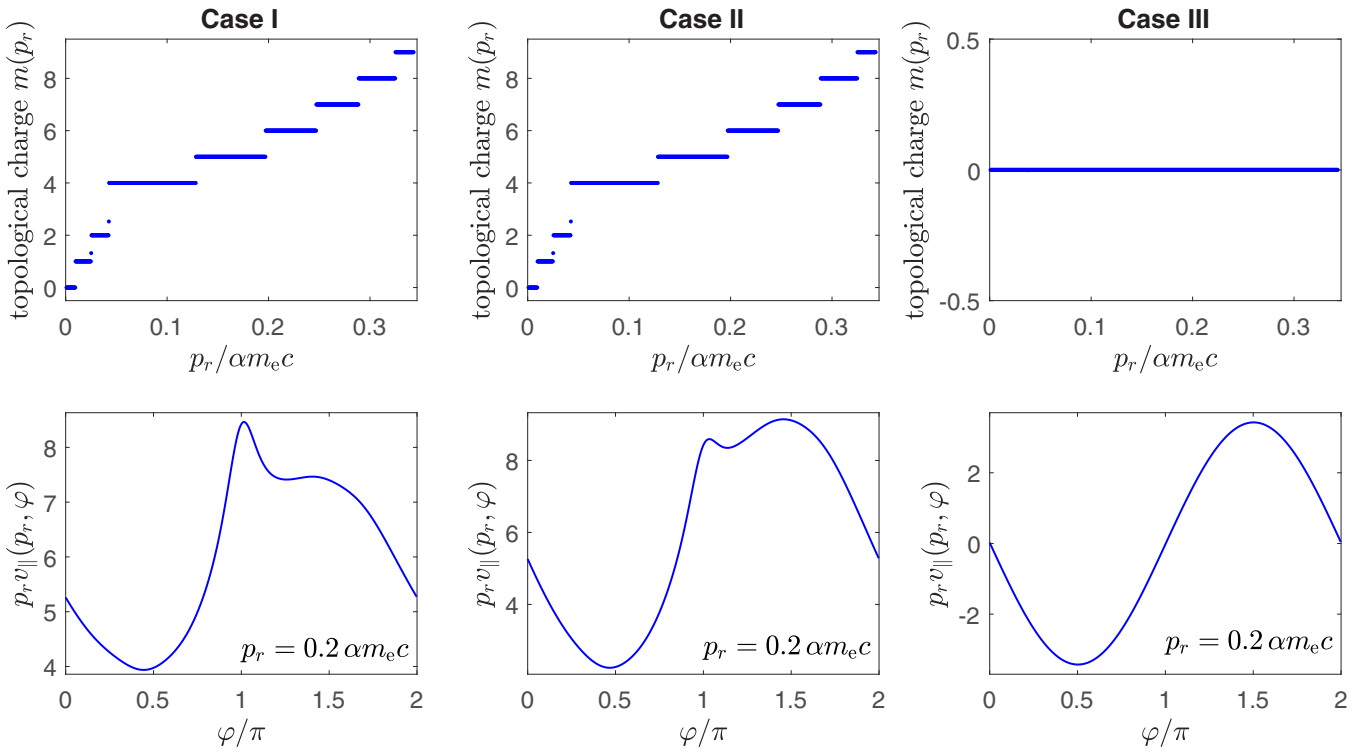

FIG. 6. Topological charge $m(p_r)$ [Eq. (21)] as a function of p_r (upper row) and the quantity $p_r v_\parallel(p_r, \varphi)$ [Eq. (22)] as a function of φ (lower row). We use the system of coordinates defined in Eq. (20). Our results are shown for case I (left column), case II (middle column), and case III (right column).

from 0 to 2π vanishes, leading to null topological charges. This is not the case for photodetachment driven by single or corotating pulses (see the lower-left and lower-middle panels of Fig. 6). This confirms that the spiral-like patterns in the probability distribution are not necessarily related to vortices. Furthermore, by comparing the upper-left and upper-middle panels of Fig. 6, we see that the number of vortices, their position, and topological charges are already defined by the single pulse. Hence, the second corotating pulse does not affect the vortex structures.

In Fig. 7, we compare the topological charges calculated based on the SFA and TDSE for case I. There are some differences between both calculations in the low-energy region of the figure (see the red and blue lines). The differences among them is caused by a difference in the positions of vortices. On the other hand, the results from two methods completely coincide in the high-energy region. In the following, we give a simple theory to predict the positions of the staircase in that region. If an electron absorbs m photons of energy $\hbar\omega_L$, its kinetic energy becomes $\frac{p_r^2}{2m_e} = m\omega_L - U_p + E_0$, where U_p is the maximum temporal ponderomotive energy. Its helicity is m. The winding number calculated for a contour of fixed radius p_r also equals m. The step position corresponds to a destructive interference which is observed between two multiphoton peaks. For simplicity, we take the midpoint between two peaks, which results in

$$m^* = \frac{\frac{p_r^2}{2m_e} - U_p + E_0}{\omega_L} - 0.5. \tag{28}$$

In Fig. 7, we see that this simple estimate works very well in the high-energy area [the green line corresponds to Eq. (28)], although it may not be a perfect multiphoton case. In this way, we can also understand why the winding number for case III equals zero: when there is a pair of identical pulses with counter-rotating circular polarization, the electron may absorb a photon with helicity $+1$ and -1.

To summarize, we have presented an example of the photoelectron momentum distribution of the spiral-type behavior that does not exhibit a quantum vortex structure. This finding

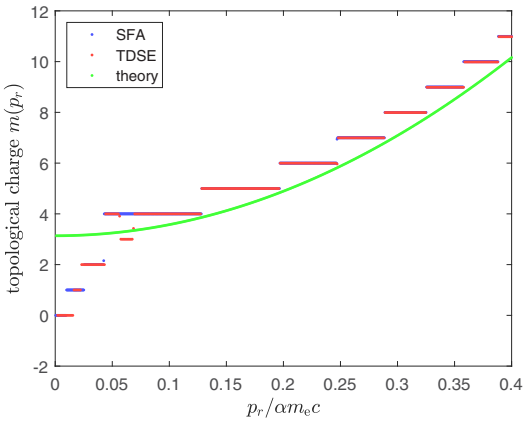

FIG. 7. Topological charges $m(p_r)$ calculated as a function of momentum p_r [Eq. (21)] from SFA (solid blue line) and TDSE (solid red line). The results concern case I, when a circularly polarized laser pulse interacts with a H^- anion. The green curve represents the prediction of Eq. (28).

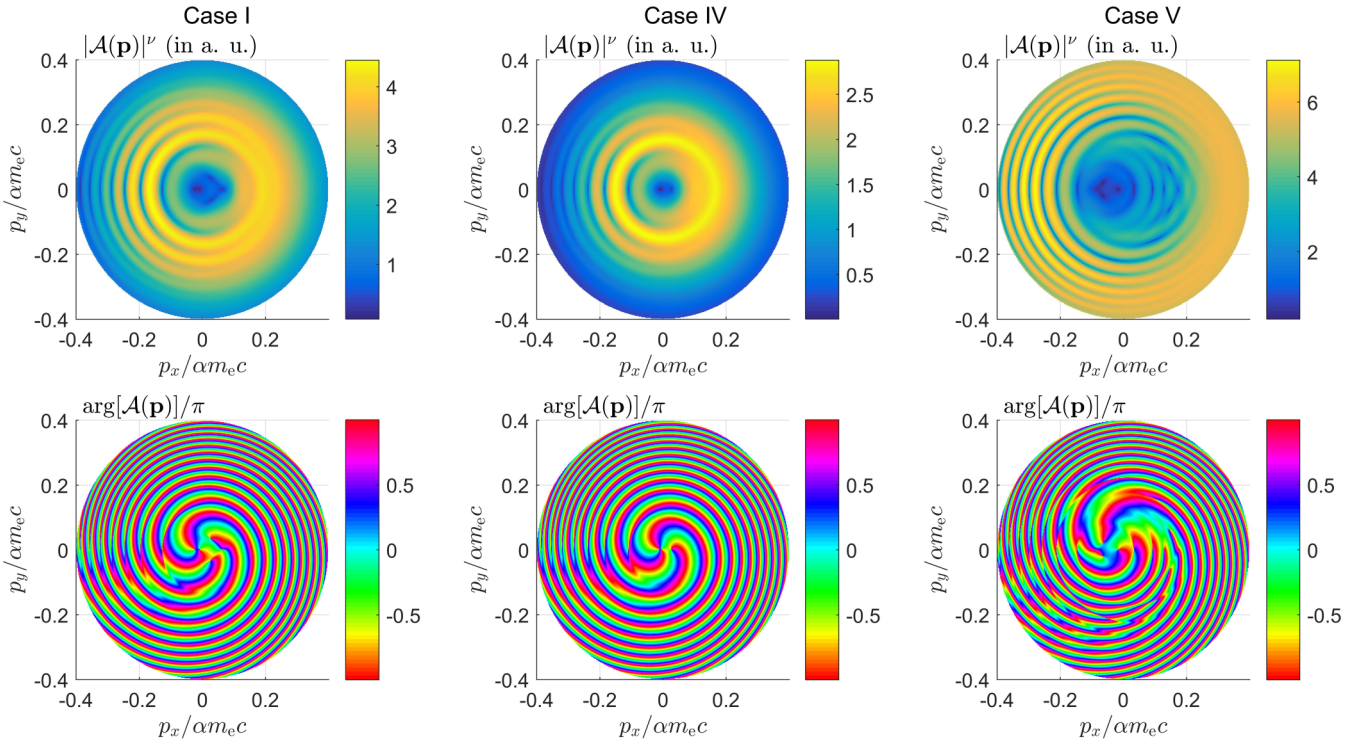

FIG. 8. Magnitude (upper row) and phase (lower row) of the probability amplitude $\mathcal{A}(\boldsymbol{p})$ calculated from the SFA formalism [Eq. (10)] in the $p_x p_y$ plane ($p_z = 0$). While the left column corresponds to case I ($I = 2.5 \times 10^{11}$ W/cm^2), the middle and right columns correspond to case IV ($I = 1 \times 10^{11}$ W/cm^2) and case V ($I = 1 \times 10^{12}$ W/cm^2), respectively. The magnitude of probability amplitudes is raised to the power $\nu = 0.5$ in order to better display details of the vortex structures.

is not necessarily universal, but indicates that the notions of spiral and vortex are not equivalent. Moreover, the lack of helix patterns does not mean the absence of vortex structures in the distribution.

V. DEPENDENCE ON THE PULSE INTENSITY

So far, we have analyzed the magnitude and phase of the probability amplitude of photodetachment obtained from both SFA and TDSE methods at the fixed pulse intensity, $I = 2.5 \times 10^{11}$ W/cm^2. The purpose of this section is to demonstrate how the intensity of the driving pulse affects the vortex structures analyzed in this paper. As has been seen, the results of TDSE are similar to those of SFA. Therefore, we only consider the SFA results in this section. For the purpose of demonstration, we only focus on case I with varied pulse intensities. Namely, we consider case IV with a lower intensity, $I = 1 \times 10^{11}$ W/cm^2, and case V with a higher intensity, $I = 1 \times 10^{12}$ W/cm^2. All other pulse parameters are the same as those in case I. In Fig. 8, we compare the magnitude and phase of the probability amplitude in cases I, IV, and V.

First, we consider the magnitude of probability distributions shown in Fig. 8. One can find that the ring with the highest amplitude moves outward with the increase of the pulse intensity. This is simply because the vector potential increases with increasing the intensity. On the other hand, the right parts of the rings merge together when the intensity increases. It can be understood through the so-called Keldysh parameter [12] $\gamma = \sqrt{|E_0|/2U_p}$, where $U_p = e^2\mathcal{E}_0^2/(4m_e\omega_L^2)$ is the maximum ponderomotive energy of the electron in the laser field and $\omega_L = N_{osc}\omega$ is the laser carrier frequency. The higher intensity means a smaller Keldysh parameter, which implies that the detachment process is closer to the picture of tunneling [29]. The Keldysh parameter in cases I, IV, and V is about 1.6, 1, and 0.5, respectively. Although case V is not a perfect tunneling case, we still cannot distinguish the multiphoton peaks on the right side of the rings.

Then, we analyze vortex structures for these three cases. First, we compare the low photoelectron momenta regimes of case I and case IV. We observe that two close vortices on the left with the topological charge $m = 1$ shown in Fig. 4 get closer, and almost emerge into a new vortex with the topological charge $m = 2$ in case IV. On the right, two vortices disappear and the node changes into a vortex with the topological charge $m = 1$ in case IV. By comparing the low photoelectron momentum regimes of case I and case V, we can find that there are many new vortex structures emerging on the right in case V. But in both cases IV and V, the vortices in the high photoelectron momentum regime remain unchanged. They are always located on the negative $\boldsymbol{e}_x$ axis.

From the above observation, we can see that the pulse intensity does not only affect the shape and magnitude of the momentum spectra, but also dramatically changes the generation and annihilation of vortex structures in the momentum space.

VI. CONCLUSIONS

We have analyzed the formation of vortices in photodetachment of H^- by circularly polarized laser pulses. Three

different cases have been considered: when the negative ion interacts with either a single pulse or pairs of identical pulses with corotating and counter-rotating circular polarizations. As we have shown, the single and corotating configurations lead to the formation of multiple vortices. This is in contrast to the case of two counter-rotating laser pulses. In this case, we have observed the spiral-like structures in the probability distribution of photoelectrons that cannot be associated with nonvanishing topological charge vortices. This statement was confirmed by calculating the topological charges $m(p_r)$, which are identically zero in the counter-rotating configuration.

In closing, we would like to emphasize a distinction between the following concepts: spiral patterns in the momentum space, electron vortex states (EVSs), and vortex structures in the momentum space. While helical patterns are frequently related to vortices, we have illustrated that no topological charge can be ascribed to them. On the other hand, EVSs, as studied for instance in Refs. [15–17] and in the review articles [19,20], do carry an intrinsic nonvanishing orbital-angular momentum ($m \neq 0$). While the probability current density of EVSs will swirl around the propagation direction of an electron, it will appear as a ringlike structure in momentum space. On contrary, the vortex structures discussed in this paper are *local* structures in the momentum space. Irrespectively of the definition of the current, in both EVS and local vortex cases, the same quantization conditions involving the current are satisfied with integer topological charge m. This is a fundamental property fulfilled by any quantum vortex, as already indicated by Dirac in [22].

ACKNOWLEDGMENTS

This work is supported by the National Natural Science Foundation of China (NSFC) under Grants No. 11961131008 and No. 11725416, by the National Key R&D Program of China under Grant No. 2018YFA0306302 (L.G. and L.P.), and by the National Science Centre (Poland) under Grants No. 2018/31/B/ST2/01251 (F.C.V.) and No. 2018/30/Q/ST2/00236 (J.Z.K. and K.K.).

L.G. and F.C.V. contributed equally to this work.

[1] J. M. Ngoko Djiokap, S. X. Hu, L. B. Madsen, N. L. Manakov, A. V. Meremianin, and A. F. Starace, Phys. Rev. Lett. **115**, 113004 (2015).
[2] K. Krajewska and J. Z. Kamiński, Phys. Rev. A **100**, 062116 (2019).
[3] K. Krajewska and J. Z. Kamiński, Phys. Lett. A **380**, 1247 (2016).
[4] J. M. Ngoko Djiokap, A. V. Meremianin, N. L. Manakov, S. X. Hu, L. B. Madsen, and A. F. Starace, Phys. Rev. A **94**, 013408 (2016).
[5] J. H. Macek, J. B. Sternberg, S. Y. Ovchinnikov, T.-G. Lee, and D. R. Schultz, Phys. Rev. Lett. **102**, 143201 (2009).
[6] J. H. Macek, J. B. Sternberg, S. Y. Ovchinnikov, and J. S. Briggs, Phys. Rev. Lett. **104**, 033201 (2010).
[7] J. M. Ngoko Djiokap, A. V. Meremianin, N. L. Manakov, S. X. Hu, L. B. Madsen, and A. F. Starace, Phys. Rev. A **96**, 013405 (2017).
[8] K. J. Yuan, S. Chelkowski, and A. D. Bandrauk, Phys. Rev. A **93**, 053425 (2016).
[9] K. J. Yuan, H. Lu, and A. D. Bandrauk, J. Phys. B **50**, 124004 (2017).
[10] D. Pengel, S. Kerbstadt, D. Johannmeyer, L. Englert, T. Bayer, and M. Wollenhaupt, Phys. Rev. Lett. **118**, 053003 (2017).
[11] S. Kerbstadt, K. Eickhoff, T. Bayer, and M. Wollenhaupt, Nat. Commun. **10**, 658 (2019).
[12] L. V. Keldysh, Sov. Phys. JETP **20**, 1307 (1965).
[13] F. H. M. Faisal, J. Phys. B: At., Mol. Opt. Phys. **6**, L89 (1973).
[14] H. R. Reiss, Phys. Rev. A **22**, 1786 (1980).
[15] F. Cajiao Vélez, J. Z. Kamiński, and K. Krajewska, Phys. Rev. A **101**, 053430 (2020).
[16] F. Cajiao Vélez, K. Krajewska, and J. Z. Kamiński, Phys. Rev. A **97**, 043421 (2018).
[17] K. Krajewska, F. Cajiao Vélez, and J. Z. Kamiński, J. Phys.: Conf. Ser. **1206**, 012002 (2019).
[18] I. Białynicki-Birula, M. Cieplak, and J. Kamiński, *Theory of Quanta* (Oxford University Press, New York, 1992).
[19] S. M. Lloyd, M. Babiker, G. Thirunavukkarasu, and J. Yuan, Rev. Mod. Phys. **89**, 035004 (2017).
[20] K. Y. Bliokh, I. P. Ivanov, G. Guzzinati, L. Clark, R. Van Boxem, A. Béché, R. Juchtmans, M. A. Alonso, P. Schattschneider, F. Nori, and J. Verbeeck, Phys. Rep. **690**, 1 (2017).
[21] I. Białynicki-Birula, Z. Białynicka-Birula, and C. Sliwa, Phys. Rev. A **61**, 032110 (2000).
[22] P. A. M. Dirac, Proc. R. Soc. London, Ser. A **133**, 60 (1931).
[23] M. V. Berry, Proc. R. Soc. London, Ser. A **392**, 45 (1984).
[24] G. F. Gribakin and M. Yu. Kuchiev, Phys. Rev. A **55**, 3760 (1997).
[25] D. M. Wolkow, Z. Phys. **94**, 250 (1935).
[26] K. Krajewska, F. Cajiao Vélez, and J. Z. Kamiński, *Advances in Optics: Reviews* (IFSA, Barcelona, 2018), Vol. 2.
[27] K. Krajewska and J. Z. Kamiński, Phys. Rev. A **94**, 013402 (2016).
[28] F. Cajiao Vélez, J. Z. Kamiński, and K. Krajewska, J. Phys.: Conf. Ser. **999**, 012005 (2018).
[29] G. Gibson, T. S. Luk, and C. K. Rhodes, Phys. Rev. A **41**, 5049 (1990).